

Assessment of a fictitious domain method for patient-specific biomechanical modeling of press-fit orthopaedic implantation

L. F. Kallivokas^{1,*}, S.-W. Na¹, O. Ghattas², B. Jaramaz³

¹ Department of Civil Engineering, The University of Texas at Austin, Austin, TX 78712, USA

² Laboratory for Mechanics, Algorithms, and Computing,
Department of Biomedical Engineering and Department of Civil and Environmental Engineering,
Carnegie Mellon University, Pittsburgh, PA 15213, USA

³ Institute for Computer Assisted Orthopaedic Surgery,
The Western Pennsylvania Hospital, Pittsburgh, PA 15224, USA

SUMMARY

In this paper we discuss an application of the fictitious domain method to the numerical simulation of the mechanical process induced by press-fitting cementless femoral implants in total hip replacement surgeries. Here, the primary goal is to demonstrate the feasibility of the method and its advantages over competing numerical methods for a wide range of applications for which the primary input originates from CT-[†], MRI-[‡], or other regular-grid medical imaging data. For this class of problems the fictitious domain method is a natural choice, because it avoids the segmentation, surface reconstruction, and meshing phases required by unstructured geometry-conforming simulation methods. We consider the implantation of a press-fit femoral artificial prosthesis as a prototype problem for sketching the application path of the methodology. Of concern is the assessment of the robustness and speed of the methodology, for both factors are critical if one were to consider patient-specific modeling. To this end, we report numerical results that exhibit optimal convergence rates and thus shed a favorable light on the approach. Copyright © 2004 John Wiley & Sons, Ltd.

KEY WORDS: Fictitious domain method; regular and geometry-conforming finite element methods; press-fit implant; linear elasticity; CT- or MRI-scan; medical imaging

1. INTRODUCTION

Today, in total hip replacement surgeries, typical pre-operative planning systems are based on geometric templating capabilities that are used invariably to find an appropriate match between the femoral and acetabular implants and their respective receiving bony structures

* Correspondence to: Department of Civil Engineering, The University of Texas at Austin, 1 University Station, C1748 Austin, TX 78712, USA (e-mail: loukas@mail.utexas.edu)

Contract/grant sponsor: National Science Foundation; contract/grant number: IIS-9422734, ATM-0326449

[†]CT: Computed Tomography.

[‡]MRI: Magnetic Resonance Imaging.

(e.g. Fig. 1). Femoral implant choices can be roughly classified into cementless and cemented: the latter refer to femoral implants whose bonding to the receiving femoral canal is ascertained via a bonding agent (“cement”), whereas the former refer to bonding ascertained via press-fitting an over-sized implant. In either case, the primary intent is to allow for an as-normal-as-possible post-operative range of motion as the healthy anatomy would have provided. Here the focus is on cementless implants: for these, by and large, it is the anatomical geometry, coupled with the experience of the operating surgeon, that dictates the implant choice, without the desirable benefit of an *a-priori* estimate of the stresses induced to the bones due to such a choice.

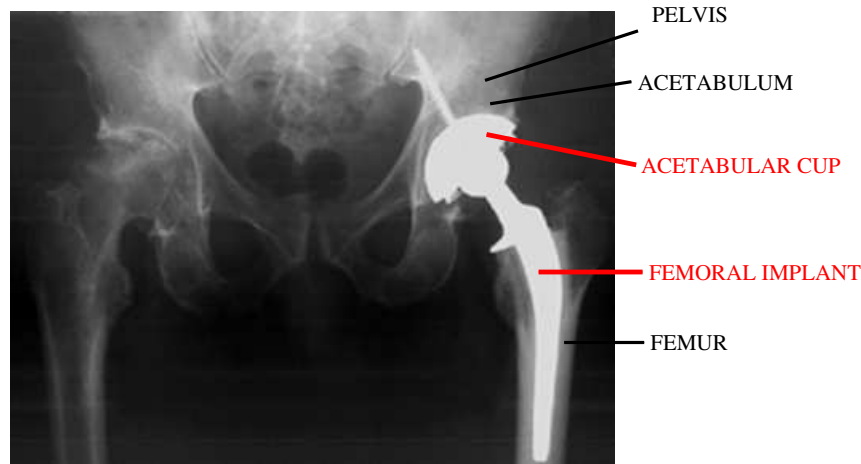


Figure 1. Typical post-operative total hip replacement x-ray; shown are the patient's acetabulum, femur, acetabular cup and femoral implant

If, however, a biomechanical feedback mechanism were to exist that would present, in a way meaningful to the planning surgeon, the potential mechanical effects of a specific implant choice, it is then conceivable that such a mechanism would act as a safety feature [1]. Its introduction might prevent selections leading to either short- or long-term failures of the chosen implant, and thus to a potential improvement of the clinical outcome[§]. The recent introduction of robotic systems in the operating room [2] —responsible for preparing the femoral cavity receiving the implant— only accentuated the need for pre-operative planners enhanced with such a biomechanical feedback mechanism. However, the inclusion of a feedback module into a pre-operative system imposes severe demands for computational speed and robustness of the underlying geometry and analysis modeling tools, especially if one were to consider the onerous requirements of patient-specific modeling. It is within the above framework that we explore in this paper the applicability and suitability of the fictitious domain method as part of an analysis tool of a biomechanical feedback mechanism for a pre-operative surgical planner.

[§] Bone typically regenerates and in many cases will grow into the porous surface of an implant; such long-term post-operative bone “remodeling” processes are not taken into account in the analysis of the short-term intra-surgical processes presented herein.

A first step in any attempt to address the mechanical (e.g. stress) effects of the implantation process has perforce to start from the reconstruction of the femoral geometry. Thus, one strategy for patient-specific geometric modeling is to develop solid models of bone volumes by reconstructing CT data, and then use these models to generate physical models appropriate for simulation (e.g. using finite element meshes within the encompassed volumes). The steps to such a process are pictorially depicted in Fig. 2. Invariably one starts from slices of the anatomical geometry obtained using patient CT-scans that result in a series of planar tomographic images. Next, the collected images undergo noise-filtering to remove artifacts. Extraction of bony boundaries (segmentation) is accomplished by edge detection algorithms, often based on density threshold values, yielding contours on each tomographic cross-section that typically separate the cortical (hard) from the cancellous (spongy) bone (red rectangle in Fig. 2). Having identified the bony geometry on the planar slices, the next step involves the reconstruction of the three-dimensional anatomy (surface reconstruction step; blue rectangle in Fig. 2) by connecting the contours extracted in the previous step (often achieved via triangulation). Once the three-dimensional reconstruction has been completed, one also needs to identify the femoral canal volume (receiving the implant), the surrounding bony volume, while also simulating the femoral neck osteotomy that will result in a modified solid model volume (green rectangle in Fig. 2). The insertion of the implant (selection is made pre-operatively, and a solid model for the implant is constructed as per the black rectangle in Fig. 2) will result in the intersection of the bone volumes identified in the previous step, leading to the final solid model. The last step, following a conventional finite element modeling approach, involves the meshing of the final solid model and, given loads, material properties, and boundary conditions, the subsequent simulation of the press-fit problem.

The process described thus far is an exacting one, plagued also by uncertainty with respect to whether the underlying algorithms could always deliver a final solid model—a hard requirement for patient-specific modeling: for example, the three-dimensional surface reconstruction step from the planar slices may not always admit a unique solution. More importantly though, there are many sources of error introduced at every step of the outlined process: these include CT imaging errors, boundary extraction errors, surface generation errors, and meshing errors. Furthermore, the surface reconstruction and the intersection of volumes during the insertion of the implant (neck osteotomy and canal preparation) result in geometrically complex volumes, characterized by fine geometric features, that are difficult to mesh using unstructured techniques, if at all possible (fine features typically drive, at least locally, three-dimensional meshers), given a reasonable set of computational resources—both hardware and software.

We remark that in this process the CT-scan data are perforce considered as the best anatomical information that is available for modeling—a sort of a ground truth. The approximation errors that are introduced during the outlined modeling path, and prior to the simulation, potentially distort that ground truth ([3]). Therefore, if one were to avoid the accumulation of these errors, while simultaneously resolving or sidestepping the meshing difficulties without sacrificing computational speed or accuracy, one would obtain a fast and robust simulation tool capable of addressing the needs of patient-specific modeling. We turn to the *fictitious domain method* in search for such a tool and use figure 3 to sketch the alternative modeling path.

Accordingly, we operate directly on the original three-dimensional voxel data, without going through the steps of segmentation and three-dimensional surface reconstruction. The boolean operations of the neck osteotomy and of the implantation are performed by imposing traction

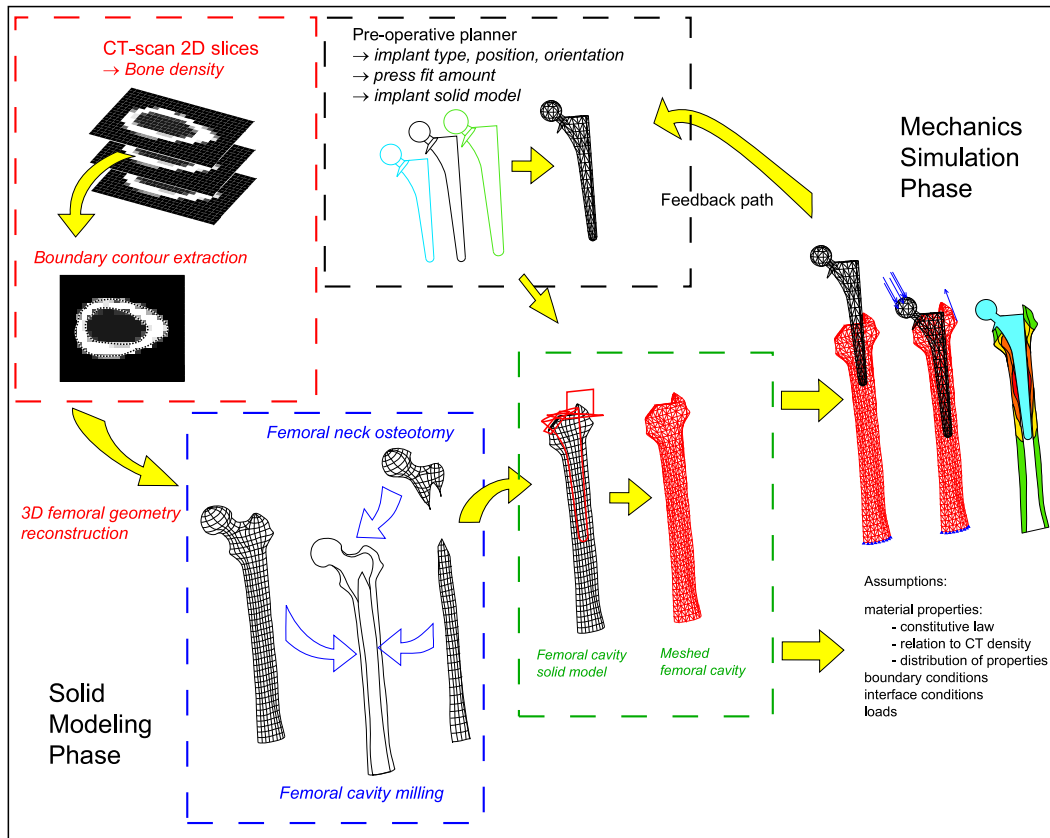


Figure 2. Typical modeling sequence based on unstructured meshes

and displacement constraints on the surface (γ) of the cutting planes and of the implant (assumed rigid), respectively. The solution for the stresses exterior to the implant surface and within the bony domain are obtained by direct application of the fictitious domain method on the original grid provided by the CT-scan. Thus, we summarily bypass all the geometric, image processing, solid modeling, and meshing errors/difficulties outlined earlier. In the next sections we provide the technical details.

2. BACKGROUND

To fix ideas we turn to the two-dimensional counterpart of the problem described in the Introduction: figure 4 depicts a slice of a patient's femur, where the shades of gray in the pixels correspond to different densities. The circular insert (red) in Fig. 4 represents the (cross-sectional) boundary of a rigid implant press-fitted into the femoral canal; the region interior to the circular boundary is occupied, post-interventionally, by the metallic implant (not shown). Given a preset amount for the press-fit, and a material description afforded by the CT-scan,

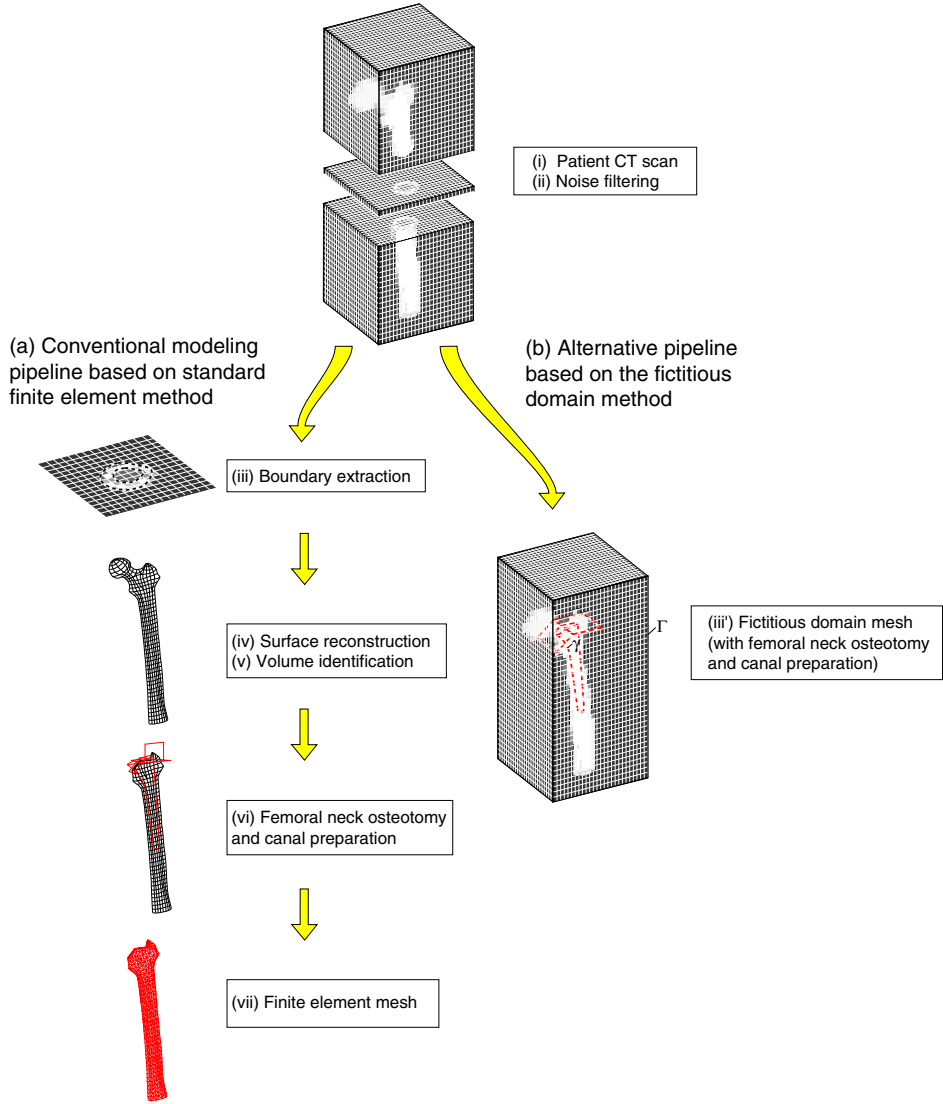


Figure 3. Modeling sequence based on conventional finite element meshes versus regular grids (fictitious domain)

the goal is to determine the displacement and/or stress field in the exterior of the implant, i.e., within the affected part of the femur. We remark, that the pixel data are provided, as it is typical the case, on a regular grid. Thus, as argued, the problem lends itself naturally to a fictitious domain formulation. Let Ω denote the entire square two-dimensional domain depicted in Fig. 4 bounded by Γ ; let ω denote the “small” circular domain bounded by γ and fully embedded within Ω . Let $\mathbf{u}(\mathbf{x})$ denote the vector displacement field in $\Omega \setminus \omega$; we seek \mathbf{u} , such that:

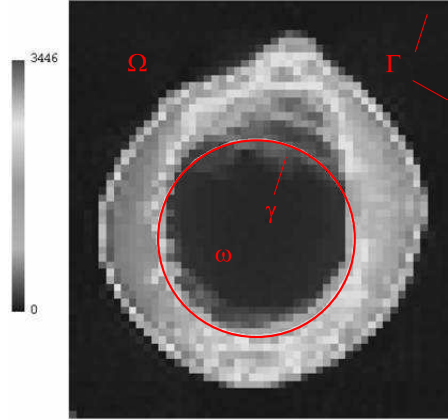


Figure 4. Typical grayscale femoral cross-section CT-scan

$$\operatorname{div} \boldsymbol{\sigma} + \mathbf{f} = \mathbf{0}, \quad \text{in } \Omega \setminus \omega, \quad (1)$$

$$\mathbf{u} = \mathbf{g}, \quad \text{on } \gamma, \quad (2)$$

$$\boldsymbol{\sigma} \boldsymbol{\nu} = \mathbf{0}, \quad \text{on } \Gamma, \quad (3)$$

where customary notation has been used to denote the stress tensor $\boldsymbol{\sigma}$, the traction vector $\boldsymbol{\sigma} \boldsymbol{\nu}$ on Γ , with $\boldsymbol{\nu}$ the outward normal to Γ ; \mathbf{g} represents the Dirichlet datum on γ (press-fit amount); and \mathbf{f} denotes body forces. In addition, under the simplifying assumption of linear elastic isotropic behavior[¶], there also hold:

$$\boldsymbol{\sigma} = 2\mu \boldsymbol{\epsilon} + \lambda \mathbf{I} \operatorname{tr} \boldsymbol{\epsilon}, \quad (4)$$

$$\boldsymbol{\epsilon} = \frac{1}{2} (\nabla \mathbf{u} + \nabla \mathbf{u}^T), \quad (5)$$

where, $\boldsymbol{\epsilon}$ denotes the small-strain tensor, \mathbf{I} the second-order identity tensor, and λ, μ are the Lamé constants.

Following classical lines of fictitious domain methods, the strong form (1)-(3), together with the constitutive relation (4) and the kinematic condition (5), can be recast as: find $\hat{\mathbf{u}}$ in Ω ,

[¶]The cortical bone's behavior is closer to an orthotropic material; here we opted for a linear elastic model for simplicity, even though the presented methodology is not limited to linear elastic materials.

such that:

$$\operatorname{div} \hat{\boldsymbol{\sigma}} + \hat{\boldsymbol{f}} = \mathbf{0}, \quad \text{in } \Omega, \quad (6)$$

$$\hat{\boldsymbol{u}} = \boldsymbol{g}, \quad \text{on } \gamma, \quad (7)$$

$$\hat{\boldsymbol{\sigma}} \boldsymbol{\nu} = \mathbf{0}, \quad \text{on } \Gamma, \quad (8)$$

with

$$\hat{\boldsymbol{\sigma}} = 2\mu \hat{\boldsymbol{\epsilon}} + \lambda \boldsymbol{I} \operatorname{tr} \hat{\boldsymbol{\epsilon}}, \quad (9)$$

$$\hat{\boldsymbol{\epsilon}} = \frac{1}{2} \left(\nabla \hat{\boldsymbol{u}} + \nabla \hat{\boldsymbol{u}}^T \right), \quad (10)$$

where $\hat{\boldsymbol{f}}$ represents an extension of \boldsymbol{f} over the entire domain Ω , such that the following restriction holds:

$$\hat{\boldsymbol{f}}|_{\Omega \setminus \omega} \equiv \boldsymbol{f}. \quad (11)$$

It can then be shown (e.g. [8]) that the restriction of the solution $\hat{\boldsymbol{u}}$ over $\Omega \setminus \omega$ coincides with the solution to the original problem defined only over the region exterior to γ , i.e.:

$$\hat{\boldsymbol{u}}|_{\Omega \setminus \omega} \equiv \boldsymbol{u}. \quad (12)$$

A statement similar to (12) can be written for $\hat{\boldsymbol{u}}|_{\omega}$, had the original problem (1)-(5) been cast over the interior to γ domain ω . In fact, we will return to the interior problem in the next section. We remark that recasting the problem over the entire domain Ω (versus the exterior to γ only), offers the advantage of using a regular discretization over Ω , as opposed to a geometry-conforming mesh in $\Omega \setminus \omega$, while weakly imposing the Dirichlet condition (7) on γ . In this way, we bypass the need for identifying material boundaries (they are implicit in the pixel data), by directly operating on the naturally regular grid provided by the CT-scan.

The weak imposition of the Dirichlet datum on γ via Lagrange multipliers gives rise to a saddle-point problem. The treatment of problems of this kind can be traced back to the mid-to late-seventies: in [4] Fix presented, under the heading of “hybrid” finite element methods, the, possibly, earliest treatment of what later became known as fictitious domain method. In [4], second-order elliptic problems were treated and *a-priori* error estimates were provided. Similarly early and parallel developments can also be found in the (then) Soviet literature (see, for example, [5, 6]). The theoretical underpinnings borrow largely from earlier developments in mixed methods [7]. Renewed interest in fictitious domain methods in the mid-nineties and later was fueled a) by the increasing need to solve three-dimensional problems efficiently (three-dimensional unstructured quality meshing remains an open problem); and b) by the maturation of fast solvers for regular grid problems. Representative works include the many contributions of Glowinski and his collaborators on flows with rigid bodies [9, 10, 11] and on other elliptic problems [12, 13] (see also [14]). Applications of the fictitious domain method cover a now ever widening spectrum, including work on unsteady problems [15], fluid-structure interaction [16], radiation and scattering problems for the Helmholtz operator [17, 18, 19], the recent work on the treatment of the exterior Helmholtz problem by Farhat and Hetmaniuk [20, 21, 22], and the development of distributed forms of the fictitious domain method in which the constraints are imposed over regions as opposed to interfaces [23, 24]. Applications to biomechanical problems are scantier (see [25, 26] for modeling of the aortic valve), despite the attractiveness of the method for these problems. In this paper, we built on past work [27, 28, 29], and discuss an application to linear elasticity of the fictitious domain method, also motivated by a biomechanics problem.

3. MATHEMATICAL FORMULATION

We turn first to the interior problem (the counterpart to (1)-(5)) (Fig. 5): find \mathbf{u} in ω , such that:

$$\operatorname{div} \boldsymbol{\sigma} + \mathbf{q} = \mathbf{0}, \quad \text{in } \omega, \quad (13)$$

$$\mathbf{u} = \mathbf{g}, \quad \text{on } \gamma, \quad (14)$$

$$\mathbf{t} = \boldsymbol{\sigma} \boldsymbol{\nu} = \mathbf{0}, \quad \text{on } \Gamma, \quad (15)$$

which, similarly to (6)-(10), is recast over the background domain Ω as (henceforth, we use *background* to refer to Ω , and *foreground* to refer to γ):

$$\operatorname{div} \hat{\boldsymbol{\sigma}} + \hat{\mathbf{q}} = \mathbf{0}, \quad \text{in } \Omega, \quad (16)$$

$$\hat{\mathbf{u}} = \mathbf{g}, \quad \text{on } \gamma, \quad (17)$$

$$\hat{\mathbf{t}} = \hat{\boldsymbol{\sigma}} \boldsymbol{\nu} = \mathbf{0}, \quad \text{on } \Gamma, \quad (18)$$

where $\hat{\mathbf{q}}$ now represents an extension of \mathbf{q} over the entire domain Ω , such that the following restriction holds:

$$\hat{\mathbf{q}}|_{\omega} \equiv \mathbf{q}. \quad (19)$$

It can then be shown [4, 8] that the restriction of $\hat{\mathbf{u}}$ in ω is a solution of (13)-(15). Problem (16)-(18), together with (9)-(10), can be readily cast in a weak form: we multiply (16) by an admissible function $\mathbf{v} \in H^1(\Omega)$. There results:

$$\begin{aligned} \int_{\Omega} \mathbf{v} \cdot (\operatorname{div} \hat{\boldsymbol{\sigma}} + \hat{\mathbf{q}}) d\Omega &= \int_{\Omega \setminus \omega} \mathbf{v} \cdot (\operatorname{div} \hat{\boldsymbol{\sigma}} + \hat{\mathbf{q}}) d(\Omega \setminus \omega) + \int_{\omega} \mathbf{v} \cdot (\operatorname{div} \hat{\boldsymbol{\sigma}} + \hat{\mathbf{q}}) d\omega = \\ &- \int_{\Omega} \hat{\boldsymbol{\sigma}} : \nabla \mathbf{v} d\Omega + \int_{\Gamma} \mathbf{v} \cdot \hat{\mathbf{t}} d\Gamma - \int_{\gamma} \mathbf{v} \cdot \hat{\mathbf{t}}^+ d\Gamma + \int_{\gamma} \mathbf{v} \cdot \hat{\mathbf{t}}^- d\Gamma + \int_{\Omega} \mathbf{v} \cdot \hat{\mathbf{q}} d\Omega = 0, \end{aligned} \quad (20)$$

where $\hat{\mathbf{t}}^-$ and $\hat{\mathbf{t}}^+$ denote the boundary tractions on γ , computed from the interior ($-$) and the exterior ($+$) region to γ , respectively. Next, the Dirichlet condition (17) is imposed weakly on γ and, thus, we seek the pair $(\hat{\mathbf{u}}, \hat{\boldsymbol{\xi}}) \in H^1(\Omega) \times H^{-\frac{1}{2}}(\gamma)$ such that:

$$\int_{\Omega} \hat{\boldsymbol{\sigma}} : \nabla \mathbf{v} d\Omega + \int_{\gamma} \hat{\boldsymbol{\xi}} \cdot \mathbf{v} d\gamma = \int_{\Omega} \hat{\mathbf{q}} \cdot \mathbf{v} d\Omega + \int_{\Gamma} \hat{\mathbf{t}} \cdot \mathbf{v} d\Gamma, \quad (21)$$

$$\int_{\gamma} \boldsymbol{\zeta} \cdot \hat{\mathbf{u}} d\gamma = \int_{\gamma} \boldsymbol{\zeta} \cdot \mathbf{g} d\gamma, \quad (22)$$

where, physically, $\hat{\boldsymbol{\xi}}$ denotes the traction jump on the γ boundary, i.e.:

$$\hat{\boldsymbol{\xi}} = [\hat{\mathbf{t}}^+ - \hat{\mathbf{t}}^-]. \quad (23)$$

The last term in (21) vanishes as per (18), and equation (22) represents the weak imposition of the Dirichlet condition (17), where $\boldsymbol{\zeta} \in H^{-\frac{1}{2}}(\gamma)$. We remark that the same system (21)-(22) could have been obtained by considering the Lagrangian of the problem and imposing the Dirichlet condition via Lagrange multipliers $\hat{\boldsymbol{\xi}}^{\parallel}$. From (21)-(22) it also follows that one

^{||}We will be henceforth referring to $\hat{\boldsymbol{\xi}}$ as the Lagrange multipliers.

need only discretize the background domain Ω and the boundary γ without resorting to (unstructured) discretization that conforms to the boundary γ . In fact, the discretizations of Ω and γ , from a geometrical point of view, are largely independent of each other (Fig. 5). The approximations, though, for the pair of test functions (\mathbf{v}, ζ) , and the pair of trial functions

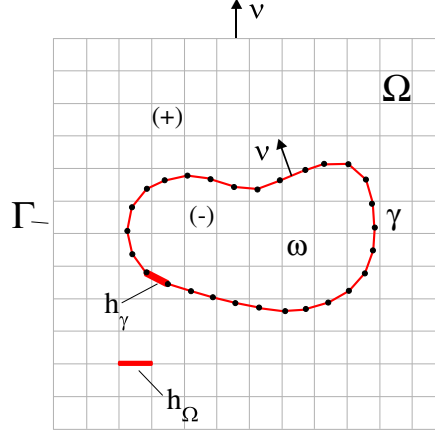


Figure 5. Regular grid (background) covering Ω with mesh metric h_Ω ; Dirichlet boundary grid (foreground) γ with mesh metric h_γ

$(\hat{\mathbf{u}}, \hat{\xi})$ cannot be independently chosen: due to the mixed nature of the problem (our unknowns are both the displacement vector and the (jump of the) tractions), the LBB (Ladysenskaja-Babuška-Brezzi) or inf-sup condition need be satisfied (e.g. [8]). Accordingly, let:

$$\hat{u}_i(\mathbf{x}) = \phi^T(\mathbf{x})U_i, \quad v_i = V_i^T \phi(\mathbf{x}), \quad \mathbf{x} \in \Omega, \quad \text{and} \quad (24)$$

$$\hat{\xi}_i(\mathbf{x}) = \psi^T(\mathbf{x})\Xi_i, \quad \zeta_i(\mathbf{x}) = Z_i^T \psi(\mathbf{x}), \quad \mathbf{x} \in \gamma, \quad (25)$$

where the subscripts $i = 1, 2$ denote cartesian components of the corresponding vectors. \mathbf{U} and Ξ denote vectors of nodal displacements in the background grid Ω and of the Lagrange multipliers on the foreground grid γ , respectively. To satisfy the LBB condition, if in (24) ϕ is chosen to be piecewise linear (quadratic), then ψ in (25) need be piecewise constant (linear). With the approximations (24)-(25), the saddle-point problem (21)-(22), upon discretization, leads to the following (indefinite) algebraic system:

$$\begin{bmatrix} \mathbf{K} & \mathbf{B}^T \\ \mathbf{B} & \mathbf{0} \end{bmatrix} \begin{bmatrix} \mathbf{U} \\ \Xi \end{bmatrix} = \begin{bmatrix} \mathbf{Q} \\ \mathbf{G} \end{bmatrix}, \quad (26)$$

where \mathbf{K} is the standard stiffness matrix arising in two-dimensional elastostatics given by:

$$\mathbf{K} = \begin{bmatrix} \mathbf{K}^{11} & \mathbf{K}^{12} \\ \mathbf{K}^{21} & \mathbf{K}^{22} \end{bmatrix}, \quad \text{with}$$

$$\mathbf{K}_{ij}^{11} = \int_{\Omega} \left[(\lambda + 2\mu) \frac{\partial \phi_i}{\partial x_1} \frac{\partial \phi_j}{\partial x_1} + \mu \frac{\partial \phi_i}{\partial x_2} \frac{\partial \phi_j}{\partial x_2} \right] d\Omega, \quad \mathbf{K}_{ij}^{12} = \int_{\Omega} \left[\lambda \frac{\partial \phi_i}{\partial x_1} \frac{\partial \phi_j}{\partial x_2} + \mu \frac{\partial \phi_i}{\partial x_2} \frac{\partial \phi_j}{\partial x_1} \right] d\Omega,$$

$$\mathbf{K}^{21} = \mathbf{K}^{12T}, \quad \mathbf{K}_{ij}^{22} = \int_{\Omega} \left[(\lambda + 2\mu) \frac{\partial \phi_i}{\partial x_2} \frac{\partial \phi_j}{\partial x_2} + \mu \frac{\partial \phi_i}{\partial x_1} \frac{\partial \phi_j}{\partial x_1} \right] d\Omega. \quad (27)$$

Similarly, the constraint matrix \mathbf{B} is given by:

$$\mathbf{B} = \begin{bmatrix} \mathbf{B}^{11} & \mathbf{0} \\ \mathbf{0} & \mathbf{B}^{22} \end{bmatrix}, \text{ with}$$

$$\mathbf{B}_{ij}^{11} = \mathbf{B}_{ij}^{22} = \int_{\gamma} \psi_i \phi_j \, d\gamma. \quad (28)$$

Furthermore, in (26) \mathbf{Q} is the vector of body forces, and \mathbf{G} is the discrete form of the right-hand side of (22). Notice that, whereas \mathbf{K} is a square matrix, \mathbf{B} , in general, is a rectangular matrix. For example, let n denote the number of grid points in Ω and let us assume that bilinear approximations are used for $\hat{\mathbf{u}}$; then \mathbf{K} will be of size $2n \times 2n$. Furthermore, let m denote the number of elements of the discretization of γ ; to satisfy the LBB condition, we use constant approximations for the Lagrange multipliers $\hat{\boldsymbol{\xi}}$ on γ , and thus \mathbf{B} will be of size $2m \times 2n$. Of course, \mathbf{B} is highly sparse, for its elements are only non-zero for those background grid cells that are intersected by γ (Fig. 6). Loosely stated and as depicted in the right column of Fig. 6, \mathbf{B} is responsible for distributing the jump of the tractions on γ to the background grid of Ω . We remark that given the regular structure of the background grid, the storage requirements

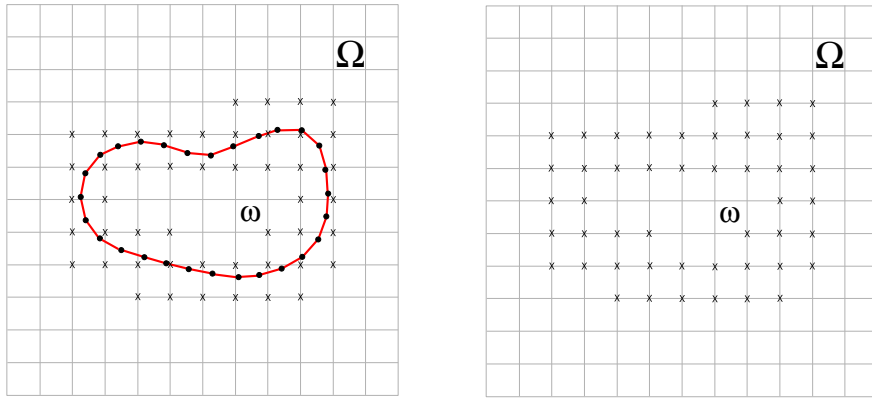


Figure 6. Schematic depiction of the role of the \mathbf{B} matrix

for \mathbf{K} can be minimized, since it is only necessary to store (even for inhomogeneous domains) only a stencil, appropriately scaled with the material parameters (λ and μ).

4. NUMERICAL RESULTS

We conducted numerical experiments with the discrete saddle-point problem (26) for a variety of problems: here we discuss the convergence rates we observed for two prototype problems involving materially homogeneous domains –an elasticity problem and a similarly-casted Laplace problem. At the end of this section we report numerical results for the original press-fit problem, that motivated this analysis, using actual patient CT-scan data.

4.1. Prototype problems

To fix ideas, we consider first the following Laplace problem (Fig. 7):

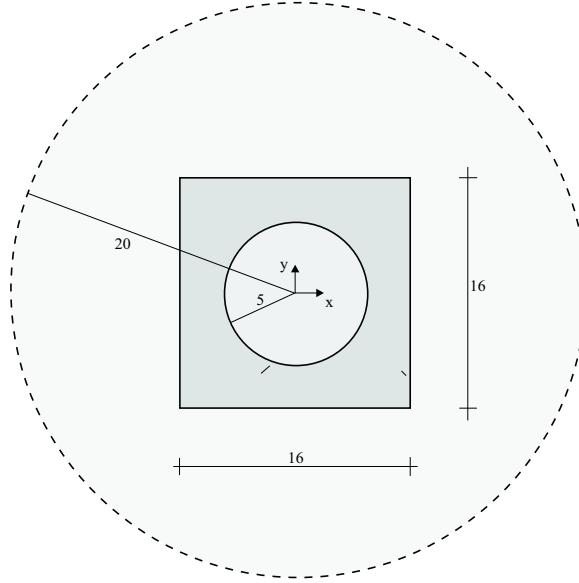


Figure 7. Domain for model Laplace problem

$$\Delta \hat{u}(x, y) = 0, (x, y) \in \Omega, \quad (29)$$

$$\hat{u}(x, y) = \cos n\theta, (x, y) \in \gamma, \quad (30)$$

$$\hat{u}(x, y) = \frac{5^n}{5^{2n} + 20^{2n}} \left[(x^2 + y^2)^{\frac{n}{2}} + \frac{20^{2n}}{(x^2 + y^2)^{\frac{n}{2}}} \right] \cos n\theta, (x, y) \in \Gamma, \quad (31)$$

where $\theta = \arctan(\frac{y}{x})$, Ω is the square $(0, 16) \times (0, 16)$ bounded by Γ , and ω is the circular domain bounded by γ for which $x^2 + y^2 \leq 5^2$. Then, the exact solution for (29)-(31) is given as:

$$\hat{u}(x, y) \equiv u(x, y) = \frac{1}{5^n} (x^2 + y^2)^{\frac{n}{2}} \cos n\theta, \text{ for } 0 \leq \sqrt{x^2 + y^2} \leq 5, \quad (32)$$

$$\hat{u}(x, y) = \frac{5^n}{5^{2n} + 20^{2n}} \left[(x^2 + y^2)^{\frac{n}{2}} + \frac{20^{2n}}{(x^2 + y^2)^{\frac{n}{2}}} \right] \cos n\theta, \text{ elsewhere.} \quad (33)$$

Furthermore, the exact solution for the Lagrange multipliers (jump in the radial derivative of u) on the circular boundary γ is:

$$\hat{\xi} = \frac{2n}{5} \frac{20^{2n}}{5^{2n} + 20^{2n}} \cos n\theta. \quad (34)$$

Problem (29)-(31) is convenient, since by controlling the value of n we can create either a smooth problem (for $n = 0$, $\hat{\xi} = 0$), or one where there will be a jump in the normal derivatives

across γ . The presence of a jump is critical to the stability of the solution and the convergence rates. The exact solution for different values of n is depicted in Fig. 8 below, whereas the exact solution for the Lagrange multipliers, for the same range of n , is shown in Fig. 14. We remark that for $n = 1, 2$, $u \in H^2(\omega)$, whereas $\hat{u} \in H^{\frac{3}{2}-\epsilon}(\Omega)$. We study first, numerically,

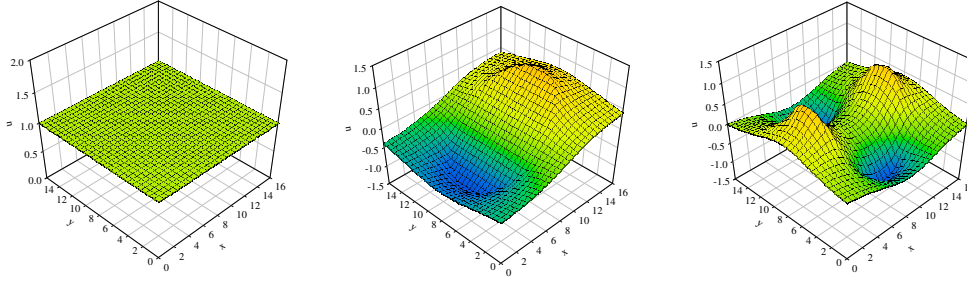


Figure 8. Exact solution \hat{u} (32)-(33) for $n = 0, 1, 2$ (left to right) (Laplace prototype problem)

the convergence rates in the L_2 norm for the solution within the inner domain ω , and on the boundary γ . We use bilinear elements for the test and trial functions of the background grid, and constant elements for the test and trial functions of the foreground grid. We use square-shaped elements for the background grid and straight-line elements for the discretization of γ . We denote with h_Ω the mesh metric for the background grid in Ω , and with h_γ the mesh metric on γ (Fig. 5).

Figures 10 show the L_2 errors for values of the $\frac{h_\gamma}{h_\Omega}$ ratio ranging from 1.6 to 22 (Fig. 10a), and 0.7 to 3 (Fig. 10b), respectively. For the error calculations shown in these figures, the foreground grid mesh is kept constant, while the background grid is refined; the small circles and squares represent computed errors, while the dashed lines represent best fits to the computed norms. To compute the reported errors we use the background grid solution for grid cells fully contained within ω ; for grid cells intersected by the straight-line approximation to the curved boundary (γ_h), we triangulate the polygon resulting from the intersections, as per Fig. 9. In this figure, shaded areas represent the integration domain for such a “boundary” cell; within each triangle we use a Gauss quadrature rule and obtain the solution at the integration points using the shape functions (bilinear) of the background grid cell and the nodal values. In this way, the solution on boundary cells is clearly affected by nodes lying outside ω , as it should.

Notice that the convergence rates in Figs. 10 are clearly suboptimal**, for both the coarser foreground grid of Fig. 10(a) and for the finer grid of Fig. 10(b). Moreover, as it can be seen from Fig. 10(b), for ratios $\frac{h_\gamma}{h_\Omega}$ approximately smaller than 2, there is no clear convergence pattern; this, numerically evaluated, critical value of the mesh metric ratio represents a stability limit. In the literature, tight estimates of the stability limit have only scantily been reported: for example, in [30], for the inf-sup condition to be satisfied the stability limit was shown to be

**For the bilinear-constant pair, we use the term optimal to refer to $O(h_\Omega^2)$ rates.

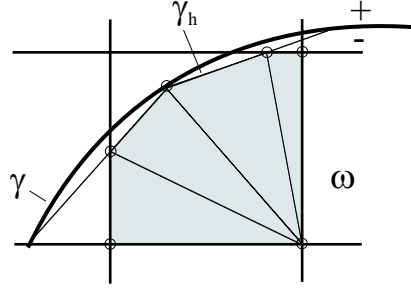


Figure 9. Typical boundary cell subdivision for error norm calculations

equal to 3, for a linear-constant pair (in [30] linear triangles were used for the background grid). On the other hand, as reported in [8], stable results were obtained using $\frac{h_\gamma}{h_\Omega} \simeq 1.5$.

By contrast, when we simultaneously refine both grids, while respecting the stability limit, i.e., when $\frac{h_\gamma}{h_\Omega} > 2$, the convergence rates improve dramatically, as shown in Figs. 11, for two different fixed ratios of $\frac{h_\gamma}{h_\Omega}$. This numerically confirms a key theoretical result from [4] that suggests that both background and foreground grids need be refined simultaneously, i.e.:

$$\frac{h_\Omega}{h_\gamma} \rightarrow 0, \text{ as } h_\Omega \rightarrow 0, h_\gamma \rightarrow 0. \quad (35)$$

The observed convergence rates are summarized in Figures 12 for the Laplace prototype problem and for two values of the harmonic parameter n . Notice that for fine discretizations, the solution, $u \equiv \hat{u}|_\omega$ or $u \equiv \hat{u}|_\gamma$ in the L_2 norm is $O(h_\Omega^2)$ (consistent with the performance reported in [8]). Shown in the same figures are the rates associated with the first-order derivatives, which, as expected, drop by one order to $O(h_\Omega)$. We remark that no *a-priori* estimates for the solution within ω have thus far appeared; moreover, even the published *a-priori* estimates for $(\hat{u}, \hat{\xi})$ over Ω differ: for example, in [4], the estimates are:

$$\|\hat{u} - u_h\|_{H^1(\Omega)} + \|\hat{\xi} - \xi_h\|_{H^{-\frac{1}{2}}(\gamma)} \leq C_0 \left(h_\Omega + h_\gamma^{\frac{3}{2}} \right), \quad (36)$$

whereas in [30] (Proposition 6), they are:

$$\|\hat{u} - u_h\|_{H^1(\Omega)} + \|\hat{\xi} - \xi_h\|_{H^{-\frac{1}{2}}(\gamma)} \leq C \left(h_\Omega^{\frac{1}{2}-\epsilon} \|\hat{u}\|_{H^{\frac{3}{2}-\epsilon}(\Omega)} + h_\gamma \left(\sum_i \|\hat{\xi}\|_{H^{\frac{1}{2}}(\gamma_i)}^2 \right)^{\frac{1}{2}} \right). \quad (37)$$

We also remark that in the presented numerical experiments the errors are mostly concentrated in the interior region ω ; very little is contributed to the global error norms $L_2(\Omega)$ from the exterior region; we attribute this to the closeness of the exterior Dirichlet boundary. Figures 13 pictorially depict the (absolute) error concentrations; notice that for the smooth problem ($n = 0$), for which there is no jump in the normal derivatives across γ ($\hat{\xi} = 0$), there is no error (the exact solution is linear). Fig. 14 depicts the quite satisfactory approximation of the Lagrange multipliers by the computed solution for a single case of $\frac{h_\gamma}{h_\Omega}$; shown in the same figure are the convergence rates for the Lagrange multipliers which exhibit

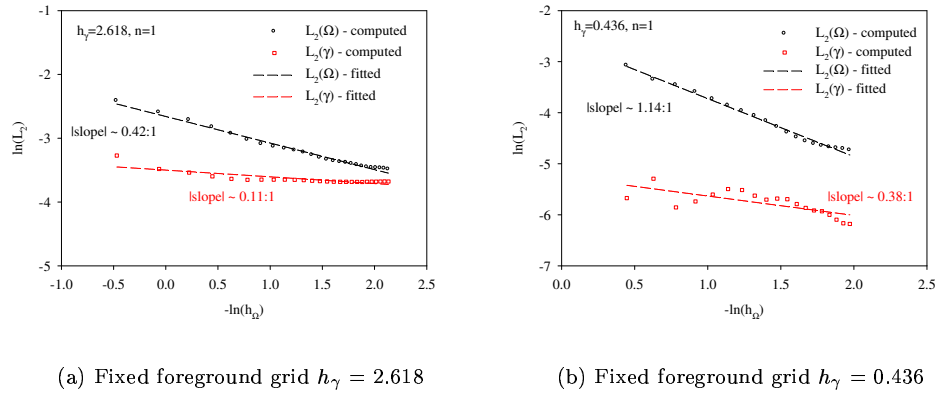


Figure 10. L_2 errors for \hat{u} in Ω and on γ ; one-sided refinement in h_Ω while h_γ is constant

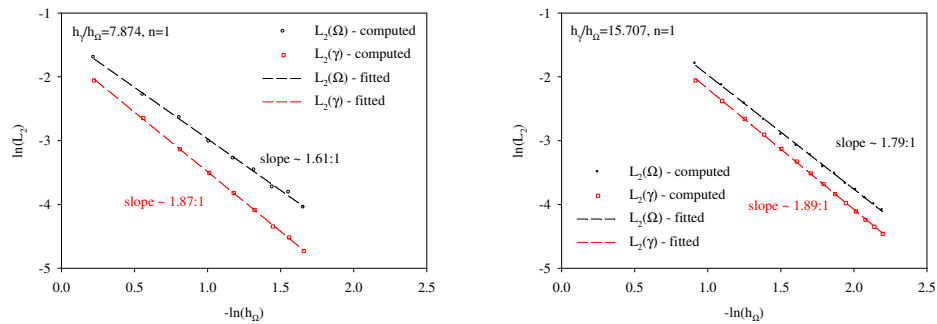


Figure 11. L_2 errors for \hat{u} in Ω and on γ ; simultaneous refinement in h_Ω and h_γ

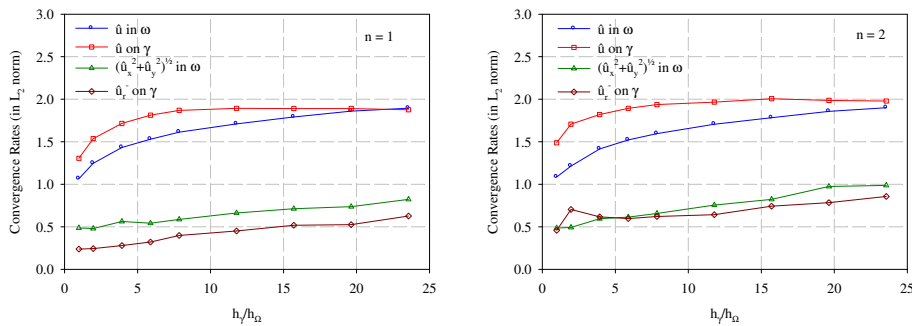


Figure 12. Convergence rates in L_2 ; simultaneous refinement; various ratios $\frac{h_\gamma}{h_\Omega}$

an $O(h_\Omega)$ performance for simultaneous refinement. We remark that convergence rates similar to the ones we discuss here also hold for the three-dimensional counterparts of the prototype problems [31].

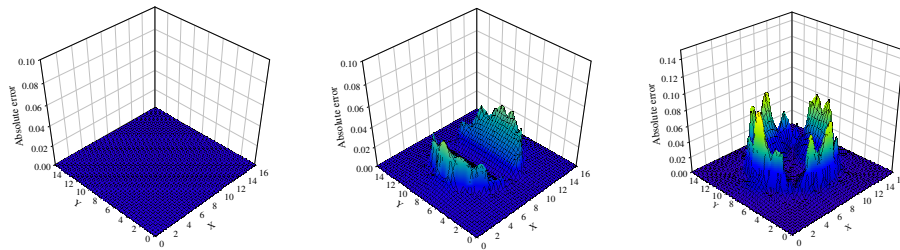


Figure 13. Absolute errors for the Laplace prototype problem; from left to right $n = 0, 1, 2$

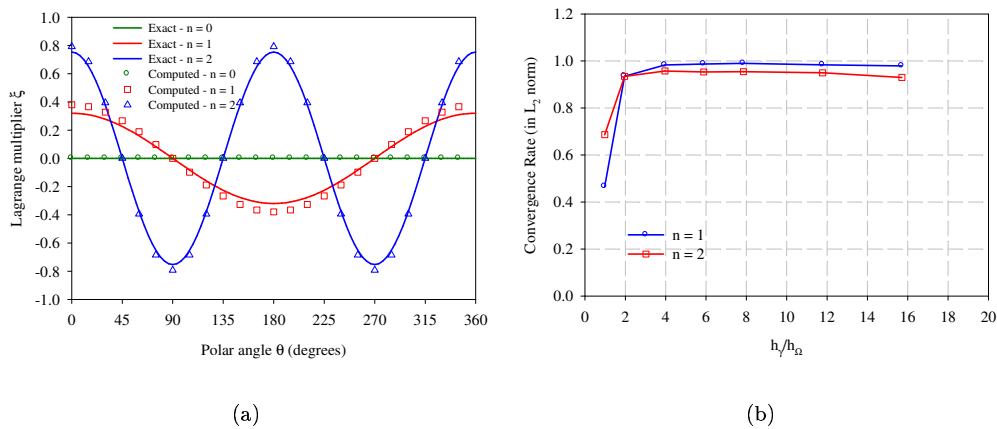


Figure 14. (a) Exact and approximate traces of the Lagrange multipliers $\hat{\xi}$ (34) for $n = 0, 1, 2$ (Laplace prototype problem); approximate solution obtained for $\frac{h_\gamma}{h_\Omega} = 11.78$; (b) cumulative rates for $n = 1, 2$

We turn next to a prototype elasticity problem similar to (29)-(31). Referring again to Fig. 7,

we seek to find the cartesian components \hat{u}_x, \hat{u}_y of the displacement vector such that:

$$\operatorname{div} \hat{\sigma}(x, y) = 0, \quad (x, y) \in \Omega, \quad (38)$$

$$\hat{u}_x(x, y) = \cos n\theta, \quad \hat{u}_y(x, y) = -\sin n\theta, \quad (x, y) \in \gamma, \quad (39)$$

$$\hat{u}_x(x, y) = \left[c_1(x^2 + y^2)^{\frac{n-1}{2}} + c_2(x^2 + y^2)^{\frac{n+1}{2}} + c_3(x^2 + y^2)^{-\frac{n+1}{2}} + c_4(x^2 + y^2)^{-\frac{n-1}{2}} \right] \cos n\theta, \quad (x, y) \in \Gamma, \quad (40)$$

$$\hat{u}_y(x, y) = \left[-c_1(x^2 + y^2)^{\frac{n-1}{2}} - c_2 \frac{n(\lambda + \mu) + 2(\lambda + 2\mu)}{n(\lambda + \mu) - 2\mu} (x^2 + y^2)^{\frac{n+1}{2}} + c_3(x^2 + y^2)^{-\frac{n+1}{2}} + c_4 \frac{n(\lambda + \mu) - 2(\lambda + 2\mu)}{n(\lambda + \mu) + 2\mu} (x^2 + y^2)^{-\frac{n-1}{2}} \right] \sin n\theta, \quad (x, y) \in \Gamma, \quad (41)$$

where $\theta = \arctan(\frac{y}{x})$, $n \geq 2$, and c_1, c_2, c_3, c_4 are appropriate constants. The constants have been obtained by solving an auxiliary Dirichlet problem in the annular region defined by the inner (γ) and outer circles shown in Fig. 7, respectively, by setting the conditions on the outer circle to be $\hat{u}_x = \frac{1}{2} \cos n\theta, \hat{u}_y = -\frac{1}{2} \sin n\theta$. The boundary conditions on Γ were obtained as the restriction on Γ of the solution within the annular region^{††}. With these definitions the exact solution within ω becomes:

$$\hat{u}_x(x, y) = \left[\frac{(x^2 + y^2)^{\frac{1}{2}}}{5} \right]^{n-1} \cos n\theta, \quad (42)$$

$$\hat{u}_y(x, y) = - \left[\frac{(x^2 + y^2)^{\frac{1}{2}}}{5} \right]^{n-1} \sin n\theta,$$

while within $\Omega \setminus \omega$ is given by (38)-(39). As it can be seen from Figs. 15 and 16, the observations

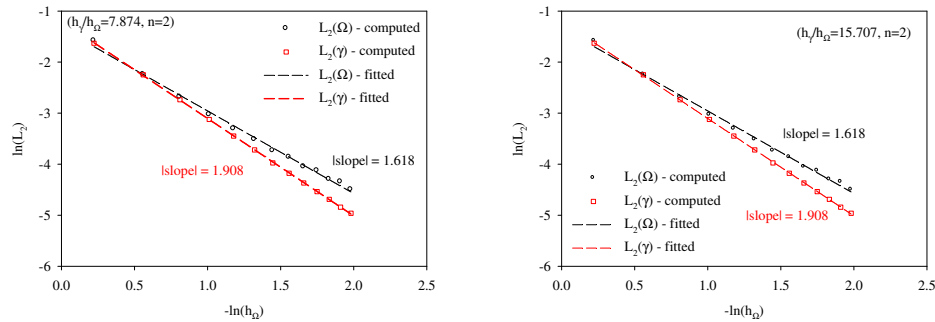


Figure 15. L_2 errors for simultaneous refinement in h_Ω and h_γ

^{††}The expressions for the constants are quite lengthy and are thus not included here; however, they can be readily obtained using any symbolic computation software package.

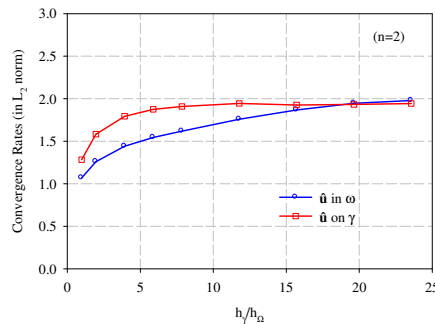


Figure 16. Convergence rates in L_2 (prototype elasticity problem); simultaneous refinement; various ratios $\frac{h_\gamma}{h_\Omega}$

made about the Laplace problem are true here as well (both problems are elliptic). Figures 15 show the convergence rates for the displacement solution on γ and in ω under simultaneous refinement with fixed ratio, while Fig. 16 shows the cumulative rates that clearly approach $O(h_\Omega^2)$ as $\frac{h_\Omega}{h_\gamma} \rightarrow 0$.

4.2. Press-fit problem over an inhomogeneous region

Next, we consider the original press-fit problem. Shown in Fig. 4 is, in grayscale, an actual adult patient CT-scan of a femoral slice; the dimensions of the square region depicted in Fig. 4 are $48\text{mm} \times 48\text{mm}$. The red insert represents the circular cross-section of a rigid implant of radius 8mm . We considered a (typical) press-fit amount of 0.5mm that was applied as a Dirichlet condition in the radial direction on γ , whereas the outer boundary Γ of the slice was taken to be traction-free.

To solve the resulting BVP, we used published correlations [32] between experimentally obtained values for Young's modulus and the CT-scan intensity, to create the material map shown in Fig. 17(a); the Poisson's ratio was assumed constant at $\frac{1}{3}$. In this map, the red regions correspond to higher values of Young's modulus, with the highest amongst them corresponding to the cortical part (exterior) of the bone. The lighter pixels between the red and blue regions at the outer fibers of the cortical bone are image artifacts. Shown in Fig 17(b) is the correspondence curves we used for Young's modulus.

We used both a finite-element approach based on a geometry-conforming mesh (Fig. 18(a)), and the fictitious domain method to solve the press-fit problem. The solid model used in the geometry-conforming mesh case was obtained by manually delineating the outer boundary of the femur. For the fictitious domain grid (Fig. 18(b)) the material properties are readily available from the CT-scan map shown in Fig. 17(a). By contrast, for each element of the geometry-conforming grid we use the coordinates of its barycenter to query the structured material map shown in Fig. 17(a) in order to assign properties. Since there is overlap between the elements of the geometry-conforming and regular meshes, there are small differences between the material properties, and we expect these differences to manifest, especially in the stress distributions. Nevertheless, as argued in the introduction, the ground-truth data are represented by the CT-scan, and hence we hold the fictitious domain as the more faithful to

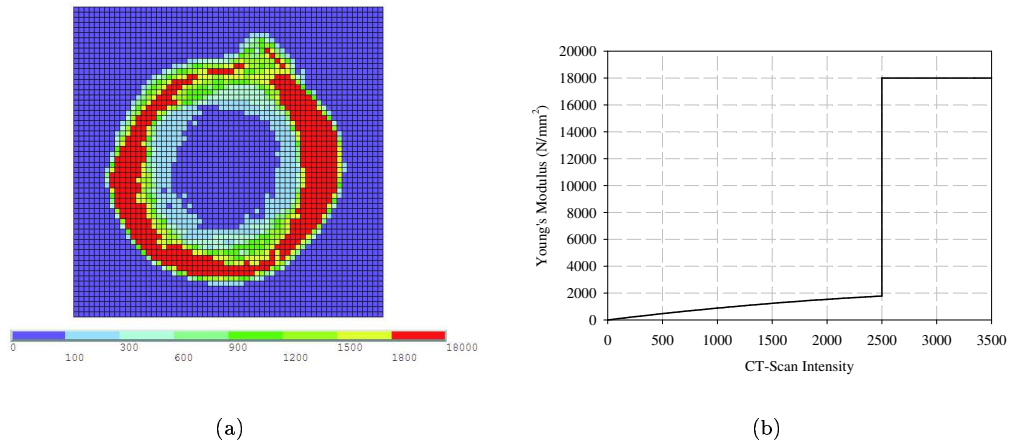


Figure 17. (a) Distribution of Young's modulus for the CT-scan of Fig. 4; (b) Young's modulus to scan intensity correlation

the original data of the two solutions.

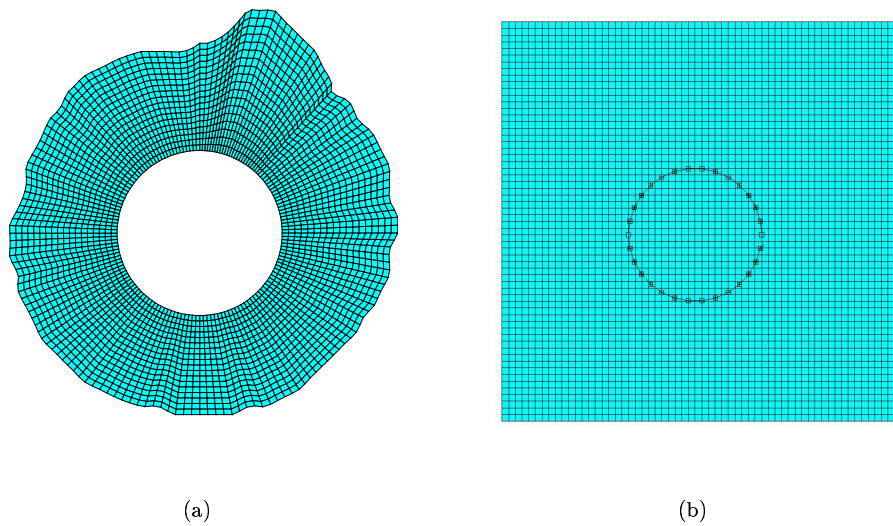


Figure 18. (a) Geometry-conforming FEM grid; (b) regular fictitious domain grid

Shown in figures 19 are the distributions of total displacements obtained using the meshes depicted in Fig. 18. Whereas, visually, both solutions appear close, Fig. 19(c) shows the pointwise difference distribution; notice that the larger differences are close to the inner boundary. For example, the highest recorded difference was 0.04 corresponding to a displacement of approximately 0.5 (8% difference). Figures 20 and 21 show similar comparisons for the σ_{xx} and σ_{yy} stress components. To ease the comparison, Fig. 22 shows the radial displacement and hoop stress on a circle of radius 15.5mm that is fully embedded within the geometry-conforming mesh of Fig. 18. Whereas the agreement between the two solutions for the displacements is excellent, differences can be seen in the stress distribution. Again, we attribute these differences, partially, to the mismatch in the underlying material properties between the two meshes. Finally, Fig. 23 shows a comparison on the displacement components along the outer boundary of the geometry-conforming grid; the agreement is quite satisfactory.

5. CONCLUSIONS

In this paper, motivated by the needs of patient-specific modeling arising in computer-assisted orthopaedic surgery, we presented a methodology for tackling problems for which the material profile originates from medical imaging data that are typically delivered on regular grids. For such problems, the fictitious domain method is a natural choice, because it avoids the segmentation, surface reconstruction, and meshing phases required by unstructured geometry-conforming simulation methods. Using prototype problems, we presented numerical results that, exhibit optimal convergence rates in the domain of interest. Similarly satisfactory results were presented using actual patient CT-data for the press-fit problem arising in the cementless implantation in total-hip replacement surgeries.

REFERENCES

1. Krejčí R, Bartoš M, Dvořák J, Nedoma J, Stehlik J. 2D and 2D finite element pre- and post-processing in orthopaedy, *International Journal of Medical Informatics*, 1997; **45**:83–89
2. Kanade T, DiGioia AM, Ghattas O, Jaramaz B, Blackwell M, Kallivokas LF, Morgan F, Shah S, Simon DA. Simulation, planning, and execution of computer-assisted surgery, in *Proceedings of the NSF Grand Challenges Workshop*, Washington, DC, 1996
3. Lengsfeld M, Schmitt J, Alter P, Kaminsky J, Leppek R, Comparison of geometry-based and CT voxel-based finite element modelling and experimental validation, *Medical Engineering and Physics*, 1998; **20**:515–522
4. Fix GM. Hybrid finite element methods, *SIAM Review*, 1976; **18**(3):460–484
5. Astrakhtantsev GP. Methods of fictitious domains for a second-order elliptic equation with natural boundary conditions, *USSR Computational Mathematics and Mathematical Physics*, 1978; **18**:114–121
6. Finogenov SA, Kuznetsov YA. Two-stage fictitious components method for solving the Dirichlet boundary value problem, *Soviet Journal Numerical Analysis and Mathematical Modelling*, 1988; **3**:301–323
7. Babuška I. The finite element method with Lagrange multipliers, *Numerische Mathematik*, 1973; **16**:179–192
8. Glowinski R, Pan T-W, Periaux J. A fictitious domain method for Dirichlet problem and applications, *Computer Methods in Applied Mechanics and Engineering*, 1994; **111**:283–303
9. Glowinski R, Pan T-W, Periaux J. A fictitious domain method for external incompressible viscous flow modeled by Navier-Stokes equations, *Computer Methods in Applied Mechanics and Engineering*, 1994; **112**:133–148
10. Glowinski R, Pan T-W, Hesla TI, Joseph DD, Periaux J. A fictitious domain approach to the direct numerical simulation of incompressible viscous flow past moving rigid bodies: application to particulate flow, *Journal of Computational Physics*, 2001; **169**:363–426

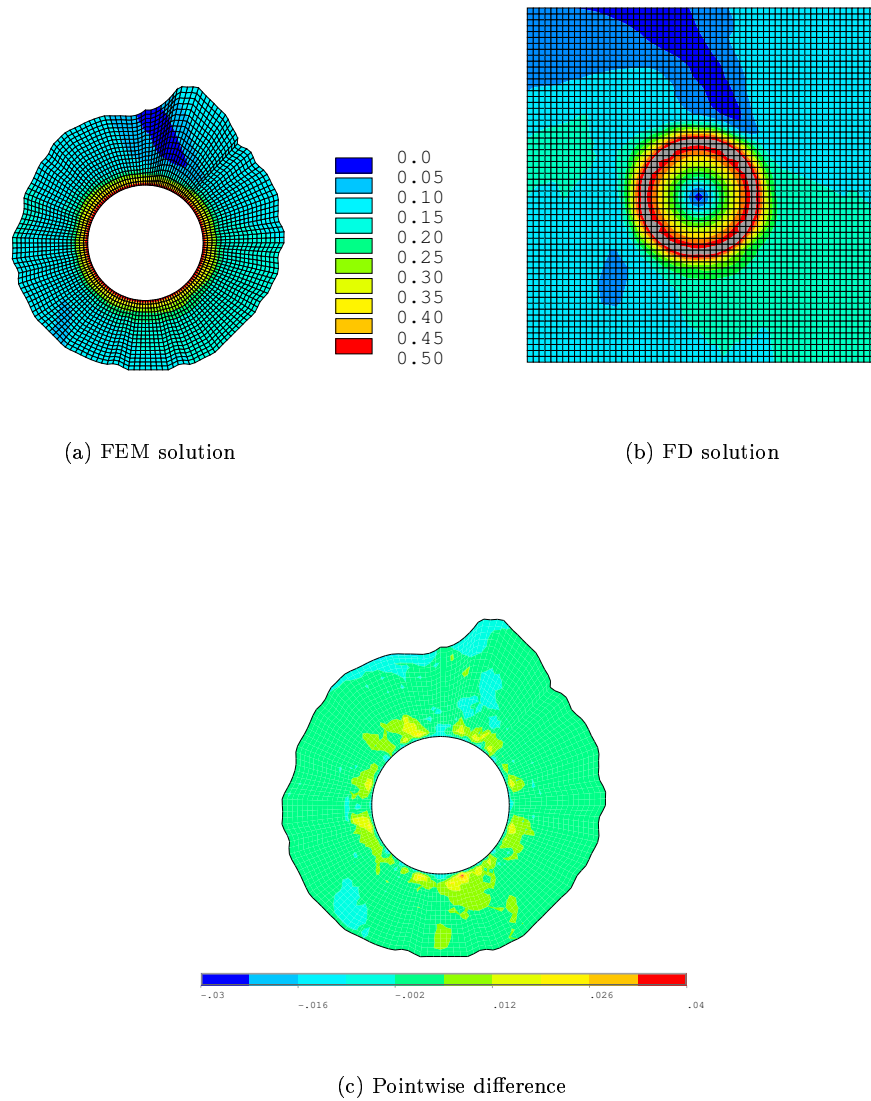


Figure 19. (a) and (b): Total displacement distribution; press-fit amount 0.5mm; (c) distribution of total displacement difference between FEM and fictitious domain; scale in mm

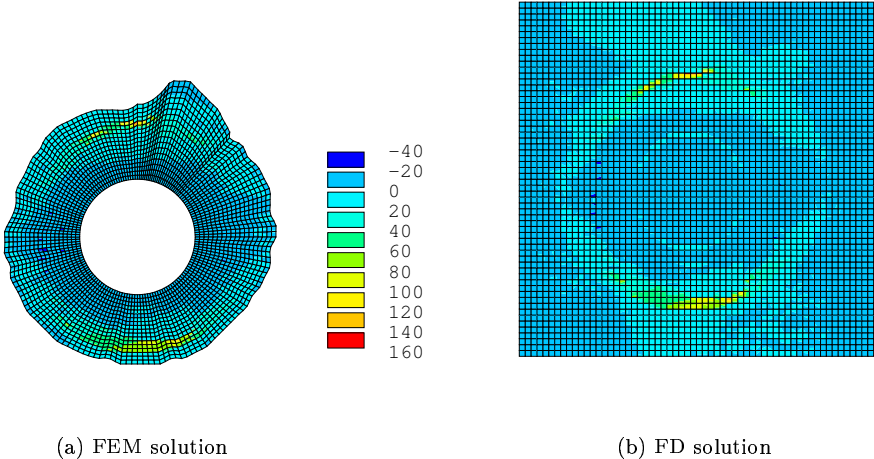


Figure 20. Distribution of σ_{xx} stresses; scale in N/mm^2

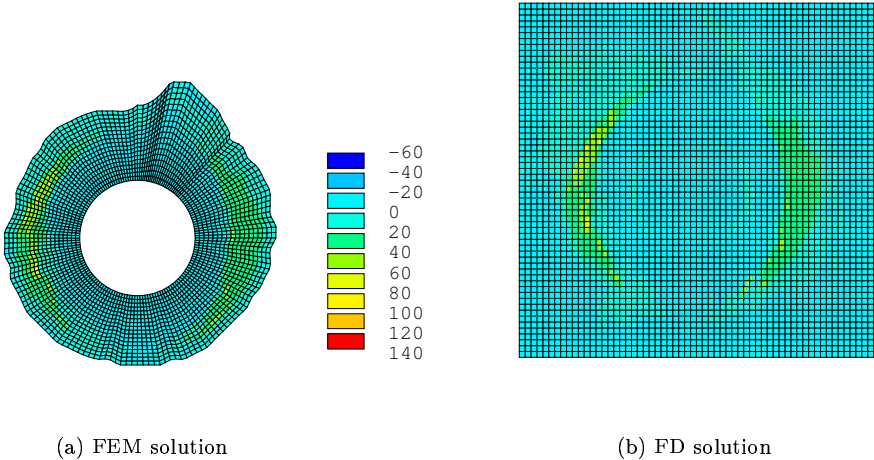


Figure 21. Distribution of σ_{yy} stresses; scale in N/mm^2

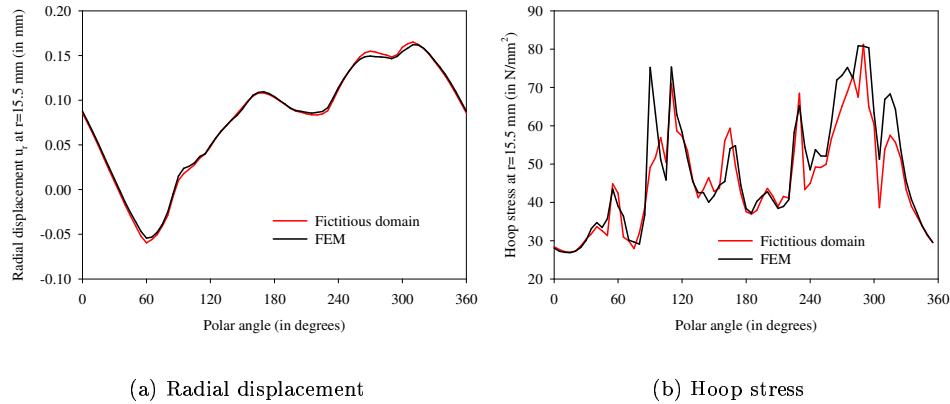


Figure 22. Comparisons of radial displacement component and hoop stress along a circle at $r = 15.5$ mm

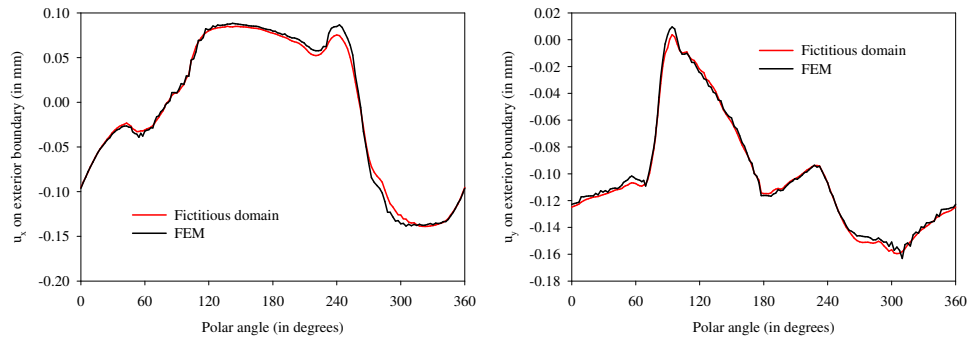


Figure 23. Comparisons of displacement components on the delineated exterior boundary

11. Glowinski R, Pan T-W, Periaux J. A Lagrange multiplier-fictitious domain method for the numerical simulation of incompressible viscous flow around moving rigid bodies, *Mathematical Problems in Mechanics*, 1997; **1**:361-369
12. Glowinski R, Pan T-W, Wells RO, Zhou X. Wavelet and finite element solutions for the Neumann problem using fictitious domains, *Journal of Computational Physics*, 1996; **126**:40-51
13. Glowinski R, Kuznetsov YA. On the solution of the Dirichlet problem for linear elliptic operators by a distributed Lagrange multiplier method, *C. R. Acad. Sci. Paris*, 1998; **1**:693-698
14. Maitre JF, Tomas L. A fictitious domain method for Dirichlet problems using mixed finite elements, *Applied Mathematics Letters*, 1999; **12**:117-120
15. Collino F, Joly P, Millot F. Fictitious domain method for unsteady problems, *Journal of Computational Physics*, 1997; **138**:907-938
16. Baaijens FPT. A fictitious domain-mortar element method for fluid-structure interaction, *International Journal for Numerical Methods in Fluids*, 2001; **35**:743-761
17. Nasir HM, Kako T, Koyama D. A mixed-type finite element approximation for radiation problems using fictitious domain method, *Journal of Computational and Applied Mathematics*, 2003; **152**:377-392

18. Heikkola E, Kuznetsov YA, Neittaanmaki P, Toivanen J. Fictitious domain methods for the numerical solution of two-dimensional scattering problems, *Journal of Computational Physics*, 1998; **145**:89–109
19. Heikkola E, Rossi T, Toivanen J. A parallel fictitious domain method for the three-dimensional Helmholtz Equation, *SIAM Journal of Scientific Computing*, 2003; **5**:1567–1588
20. Farhat C, Hetmaniuk U. A fictitious domain decomposition method for the solution of partially axisymmetric acoustic scattering problems. Part I: Dirichlet boundary conditions, *International Journal for Numerical Methods in Engineering*, 2002; **54**:1309–1332
21. Hetmaniuk U, Farhat C. A fictitious domain decomposition method for the solution of partially axisymmetric acoustic scattering problems. Part 2: Neumann boundary conditions, *International Journal for Numerical Methods in Engineering*, 2003; **58**:63–81
22. Hetmaniuk U, Farhat C. A finite element-based fictitious domain decomposition method for the fast solution of partially axisymmetric sound-hard acoustic scattering problems, *Finite Elements in Analysis and Design*, 2003; **39**:707–725
23. Glowinski R, Pan T-W, Periaux J. Distributed Lagrange multiplier methods for incompressible viscous flow around moving rigid bodies, *Computer Methods in Applied Mechanics and Engineering*, 1998; **151**:181–194
24. Patankar NA, Singh P, Joseph DD, Glowinski R, Pan T-W. A new formulation of the distributed Lagrange multiplier-fictitious domain method for particulate flows, *International Journal of Multiphase Flow*, 2000; **26**:1509–1524
25. De Hart J, Peter GWM, Schreurs PJG, Baaijens FPT. A two-dimensional fluid-structure interaction model of the aortic valve, *Journal of Biomechanics*, 2000; **33**:1079–1088
26. De Hart J, Peter GWM, Schreurs PJG, Baaijens FPT. A three-dimensional computational analysis of fluid-structure interaction in the aortic valve, *Journal of Biomechanics*, 2003; **36**:103–112
27. Shah S, Kallivokas LF, Jaramaz B, Ghattas O, DiGioia AM. The fictitious domain method for biomechanical modeling using patient-specific data: Promise and prospects, in *Proceedings of the Second International Symposium on Medical Robotics and Computer Assisted Surgery* Baltimore, MD, 1995; 329–333
28. Kallivokas LF, Jaramaz B, Ghattas O, Shah S, DiGioia AM. Biomechanics-based pre-operative planning in THR-Application of fictitious domain method, in *Advances in Bioengineering*, ASME Winter Annual Meeting, Atlanta, GA, 1996; **BED-Vol. 33**:389–390
29. Na S-W, Kallivokas LF, Jaramaz B. Modeling of a press-fit problem in computational biomechanics using the fictitious domain method, in *Proceedings 14th US National Congress on Theoretical and Applied Mechanics, Special Symposium in Advances in Computational Mechanics*, Blacksburg, VA, 2002; 313
30. Girault V, Glowinski R. Error analysis of a fictitious domain method applied to a Dirichlet problem, *Japan Journal of Industrial and Applied Mathematics*, 1995; **12**:487–514
31. Biros G, Kallivokas LF, Ghattas O, Jaramaz B. Direct CT-scan to finite element modeling using a 3D fictitious domain method with an application to biomechanics, in *Proceedings Fourth US National Congress on Computational Mechanics*, San Francisco, CA, 1997; 404
32. Mow VC, and Hayes, WC. *Basic Orthopaedic Biomechanics*, Second Edition, Lippincott-Raven Publishers, New York, 1997